INVESTIGATION OF DRAG REDUCTION MECHANISM BY MICROBUBBLE INJECTION WITHIN A CHANNEL BOUNDARY LAYER USING PARTICLE TRACKING VELOCIMETRY

YASSIN A. HASSAN* and C. C. GUTIERREZ-TORRES
Department of Nuclear Engineering
Texas A&M University
College Station
Texas 77843-3133
*Corresponding author. E-mail : y-hassan@tamu.edu

Received November 14, 2006

Injection of microbubbles within the turbulent boundary layer has been investigated for several years as a method to achieve drag reduction. However, the physical mechanism of this phenomenon is not yet fully understood. Experiments in a channel flow for single phase (water) and two phase (water and microbubbles) flows with various void fraction values are studied for a Reynolds number of 5128 based on the half height of the channel and bulk velocity. The state-of-the art Particle Tracking Velocimetry (PTV) measurement technique is used to measure the instantaneous full-field velocity components. Comparisons between turbulent statistical quantities with various values of local void fraction are presented to elucidate the influence of the microbubbles presence within the boundary layer. A decrease in the Reynolds stress distribution and turbulence production is obtained with the increase of microbubble concentration. The results obtained indicate a decorrelation of the streamwise and normal fluctuating velocities when microbubbles are injected within the boundary layer.

KEYWORDS : Drag Reduction, Microbubbles, Particle Tracking Velocimetry, Local Void Fraction

1. INTRODUCTION

Drag reduction is a complex phenomenon that has been studied for several years. The benefits of a success in drag reduction control are enormous. Reduction in drag can increase range or speed in transportation systems, reduce the energy consumption in pumping system, improve systems efficiency, and decrease fuel consumption with the indirect consequences of cost savings and decrease in pollutants emission. In addition, the interaction of microbubble with the flow in the near-wall turbulence structures in turbulent boundary layer is an important complex phenomenon. It is responsible for fluid mixing and increased heat transfer from the nuclear fuel rods to the coolants during the subcooled boiling processes. The control of these processes requires a through understanding of underlying physical mechanism. As an example, the departure of nucleate boiling predictions are less than satisfactory despite the studies and great interest they have generated over the years. In this study, isothermal microbubble boundary layer dynamics will be investigated to shed some the ubiquitous structural features in the near-wall region of turbulent boundary layers.

Polymer additives injection, surfactants injection, riblets, wall oscillations, traveling waves, blowing, and microbubbles injection within the boundary layer are among methods, which have been studied to achieve understanding of the drag reduction mechanism. Injection of microbubbles in the inner zone of the boundary layer to achieve drag reduction has been investigated since the sixties and early seventies. The environment friendly characteristics of this technique in achieving drag reduction make it an attractive method. Recently, efforts have been sparked again with a promise of achieving the goal of saving energy and mitigating the impact on the environment.

McCormick and Bhattacharyya [1] reported one of the first microbubble experimental results using electrolysis to produce hydrogen microbubbles on the hull of a submersible axisymetric body. Drag reduction values as high as 30% were obtained. Reported results showed that the amount of drag reduction depends on the speed and the rate of hydrogen production. A decrease in the Reynolds stresses was observed. Madavan et al. [2] carried out a numerical investigation of the phenomenon in an effort to clarify the effect of the presence of the microbubbles on the physical properties values (as density and viscosity) of the fluid in the boundary layer. The main conclusions presented in their work were that the microbubbles' presence in the boundary layer affects the turbulent structure by altering the local effective

viscosity and density. A strong dependence was found on the drag reduction magnitude with the bubble volumetric concentrations and their location. It was also noted that the bubbles are most effective when they are in the buffer layer. Merkle and Dutsch [3] showed that drag reduction values up to 80% could be achieved by injecting microbubbles in the boundary layer. The microbubble injection became ineffective for low speed conditions due to buoyancy. This experiment indicated the strong relationship between the drag reduction and microbubbles concentration. A new parameter was introduced in the relationship for drag reduction is the diameter of the bubbles. The role of the bubble sizes, their location and concentration within the boundary layer was considered as a significant parameter for the drag reduction magnitude. However, a complete understanding of the drag reduction mechanism using microbubbles within the boundary layer has not been attained.

Moriguchi and Kato [4] tried to elucidate the influence of microbubble diameter on the drag reduction phenomenon; however, their results seem to indicate that there is no influence of the bubble diameter on drag reduction. It will be necessary to perform more experiments to investigate the validity of this conclusion, which is contrary to other investigation findings [3, 5, 6].

Guin et al. [7] carried out experiments in a two-dimensional water channel. The microbubble production close to the wall was attained by air injection through a porous media. The results confirmed the notion that the microbubble drag reduction is an inner region dependent phenomenon.

The role of the microbubble location within the boundary layer seems to be related to the notion that microbubbles act as a disruptive element that interrupts the autonomous cycle that sustains turbulence in a region below $y^+ \approx 60$ and above $y^+ \approx 20$, [8].

After the first numerical investigation of Madavan et al. [2], there have been several efforts to simulate numerically the drag reduction by microbubbles injection phenomenon. Kanai and Miyata [9] developed the marker-density-function (MDF) method to conduct direct numerical simulation (DNS) for bubbly flows. These results indicate that microbubbles need to be injected near the wall. It pointed out the importance not only of the microbubble diameter, but also their shape as well as their distribution within the computational domain.

Recently, Xu et al. [5] considered the effects of bubble seeding levels, bubble size, and interaction with the turbulent flow and presented the results of direct numerical simulations of a turbulent channel flow that was seeded with small, rigid, spherical bubbles up to an average void fraction of 8%. Their results showed that the strongest sustained drag reduction is achieved for small bubbles and they strengthened the idea of the importance of microbubble location within the boundary layer as well as the relation of void fraction concentration values with the drag reduction.

In an effort to clarify the mechanism of drag reduction caused by microbubbles, the structure of turbulence in a channel flow with microbubbles presence is studied using a high resolution particle tracking velocimetry technique (PTV). In this study, full-field of the two-dimensional velocity components within a location close to the wall was measured. Several values of local void fraction were obtained and their effects on the drag reduction were investigated.

2. EXPERIMENTAL SETUP AND PROCEDURE

2.1 Water Channel

The experiment was carried out in a new constructed rectangular cast acrylic channel, with dimensions of 4.8 m length, 20.5 cm wide and 5.6 cm height. Water flow was circulated through a closed loop facility. First, water flowed from an upper tank, which is located about 2.02 m high above the channel level, to the channel by gravity. Then, water was transported to a lower tank, located approximately 0.5 m below the channel, from which water was pumped to the upper elevation tank. The upper tank has a constant water head maintained by the pumps. As shown in Fig. 1, at the channel entrance, a screen having a cross section of 20.4 cm x 17 cm with circular holes of 4 mm radius, spaced with a distance of 1.5 mm was used to remove large eddies. The wall channel thickness was 1.2 cm.

The water flow rates were measured by three water flow meters. Two of them are GPI electronic digital meters with a measurement range from 3 to 50 GPM. The third one is a flow meter by Dwayer with a measurement range from 0 to 10 GPM.

2.2 Pressure Measurement

The pressure gradient in the test section was measured with pressure taps positioned on the top wall of the channel over a distance of 157.5 cm. A Validyne pressure transducer (Model DP103) was used. This transducer has a range of pressure difference of 0-35 Pascal. To obtain the wall shear stress from the pressure drop measurements, the following equation is used for single phase fully developed channel flow:

$$\tau_w = -H\frac{\Delta P}{\Delta x} \tag{1}$$

where, τ_w is the wall shear stress; ΔP, is the pressure drop measured by the pressure transducer; Δx is the axial distance between the pressure connection tabs and H is the half height of the channel; this equation was employed before for drag reduction investigations in a channel flow by [10]. In this study, this measurement method was used to obtain the value for the wall shear stress for single phase flow. The calculated value of the wall shear stress is only used to validate and compare the results obtained directly from PIV. In the cases where microbubbles are generated

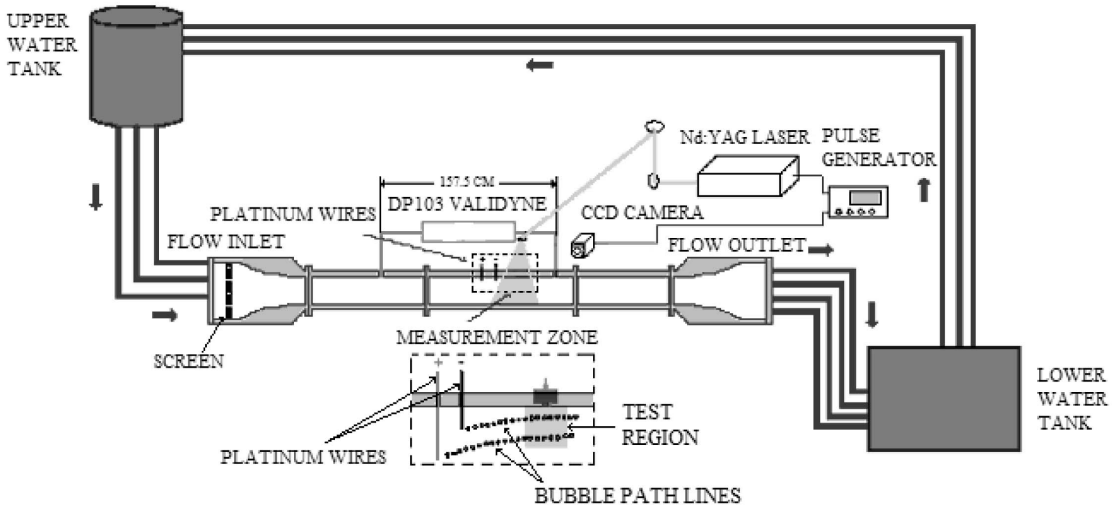

Fig. 1. Channel Set Up

and present, we emphasize that PIV velocity components were used to estimate the shear stress.

2.3 Microbubble Production

The hydrogen microbubbles used to achieve drag reduction were produced by electrolysis at 10 cm upstream the test zone. Platinum wire with a diameter of 76 μm was used as electrodes. To produce hydrogen microbubbles of 30 μm a current of 25 mA was conducted through the electrodes. The negative electrode (cathode) produces hydrogen microbubbles whereas the positive one (anode) produces oxygen microbubbles. A schematic of the channel setup illustrating the location of the wires is shown in figure 1. The subsection of the figure illustrates the path lines of the microbubbles within the test zone (shaded square area).

2.4 PIV System

The illumination source for the particle image velocimetry (PIV) system is a high power, dual oscillator Nd:YAG laser. The model is Spectra-Physics PIV-400-30. Each resonator has a fixed frequency of 30 Hz. It is possible, therefore, to run the laser system at 60 Hz. The maximum power is rated at 400 mJ per pulse, for the 532 nm wavelength (corresponding to green light), but the actual maximum output power achievable ranges from 300 to 350 mJ per pulse. The pulse width is about 7 ns.

High energy mirrors and lenses are required to transmit and shape the laser beam. Sharp images are obtained with the help of 60 mm focal length lenses, and a sheet of light of about 1mm thickness is produced and used to illuminate the viewing area. The velocity field in an x-y vertical plane is obtained by PIV at a position, L, of 3.15 m downstream from the channel inlet (L/H = 112), where H is half channel height. The particle seeds used for tracing the flow have a small diameter range of 6-9 μm with specific gravity of 1.01 close to water's specific gravity.

The scattered laser light from the seeding particles was recorded using a CCD Kodak Megaplus camera, Model Megaplus ES 1.0/10, 1008 x 1018 pixels. This camera has a 1-inch CCD array format, and the pixel size is 9 μm. The camera has the Trigger Double Exposure capability, which allows studying high velocity flows. The viewing area was 1.28 cm^2 and was located near the upper channel wall. The thickness of the sheet of green light that illuminates the viewing area is 1 mm. The system recorded 60 images per second. This results into thirty velocity fields per second. Each velocity field was obtained from a pair of consecutive images, capturing the second image of the pair 1 ms after the first one via frame straddling approach. Images were recorded for a time span of approximately 3.3 sec. The total sets of velocity fields per run were 100. Several runs were obtained with the same flow conditions.

2.5 System Synchronization

The image acquisition rate was 60 frames per second (fps) at a resolution of 1007 x 1007 pixel, although the normal frame rate of the CCD camera is only 30 fps. The increase of the camera frame rate to 60 fps is a consequence of the correct synchronization between the triggered double exposure capability of the CCD camera, and the laser system light pulsing. The synchronization was performed by the high accuracy pulse generator MFL, which has a four-channel digital delay/pulse generator. This Stanford Research Systems, Inc. pulse generator model DG535 has accuracy in the range of picoseconds. In order to achieve the 60 Hz rate, the exposure time for the first frame is

only 0.128 ms, but for the second frame the CCD array is exposed for 32.4 ms. This allows to fire the second laser light pulse at any specified time within the 32.4 ms duration. The selected time length, d Δbetween pulse 1 and pulse 2 is 1 ms. The time duration, T, between pulse 2 and pulse 3 is 32.33 ms. Clearly, this feature allows to study high turbulent flows with a high spatial resolution utilizing the analysis of a pair of successive frames as 1 and 2; 3 and 4, etc. The time, dt, between these images (odd image number first, followed by even image number) is equivalent to a virtual frequency of 1 kHz. Figure 2 shows a diagram of the synchronization and timing used during these measurements.

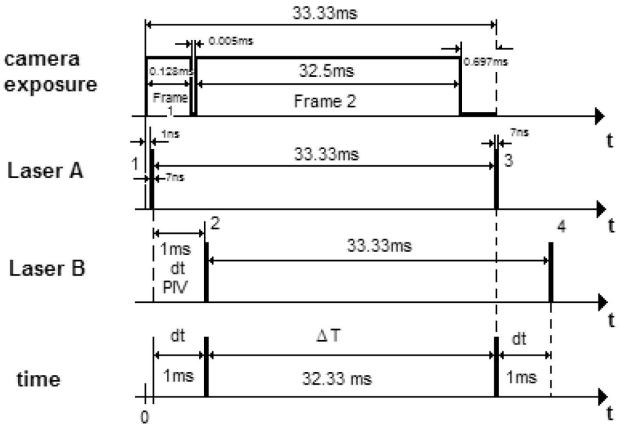

Fig. 2. Synchronization Between Laser System and CCD Camera

3. IMAGE PROCESSING

The PIV system was calibrated using a rectangular calibration target with white dots regularly distributed with spacing between adjacent dots of 2.54 mm. The calibration grid was located at the viewing plane and images were recorded. The relation between the calibration grid dots locations in camera coordinates to the coordinates in the physical plane was obtained. Theoretically, it is possible to determine such relation from the imaging parameters, such as the focal length, the angles and the distances, but this approach is mostly not applicable, because an exact knowledge of all parameters is required. This includes the actual position of the lens plane and information about lens distortions, which are normally not known and not easy to obtain.

Image preprocessing is necessary to remove background, noise, reflection effects, and other distortions that can cause possible mismatching of the tracer particles through consecutive frames. The methodology is applied to a pair of consecutive PIV images. The illumination conditions, for a consecutive pair of images may differ due to laser light intensity differences from one pulse to another; this is also due to a different exposure time for each image. An average image from the whole set of original images is calculated. Since the illumination is different for even (Laser B) and odd (Laser A) images, two separate average images are needed, one for the odd images and another for the even images. The next step is to subtract the average images from the corresponding original images. Then, these images are equalized before using the particle tracking routines or PIV analysis process.

In this study, the particle tracking was performed through a cross correlation algorithm. Two different software applications were used for the tracking process. The resulting velocity vectors from each application were then compared and combined. This hybrid tracking technique greatly increased the total number of vectors used for the flow field analysis. The first application allows for online image processing and tracking of the particle tracers. Thus, the image threshold and tracking parameters can be correctly set for a whole data set [11].

The other tracking process is an in-house routine [12], and it has been improved over the last fifteen years. It is mainly an offline application, and it runs on a UNIX environment. It requires the images be converted to ASCII files. The image processing and conversion is performed through a developed application with the LabView programming environment. The tracer particle centroid algorithm also runs in UNIX environment.

Once the velocity vectors are obtained from both particle tracking algorithms, they proceed through a filtering process. The filters are applied independently to the vector data sets from each tracking process. The first filter is related to the cross correlation value itself. In our case, only those vectors with a cross correlation coefficient value higher than the average value are considered for the flow field analysis. During this step usually about 50% of the total vectors are removed. Some of these vectors can easily be seen as erroneous vectors, i.e.; vectors with direction and/or magnitude values deviated from the neighbor vectors.

The second filter removes vectors that are not within the average +/- a standard deviation value of the magnitude and direction of the representative velocity vector within a small window, e.g. of 20x20 pixels. This step ensures that velocity gradients are correctly delineated. Then, those vectors very close to the image boundaries are also removed. In this step about 10% of the vectors are filtered out. In total, about 40% of the initially tracked vectors are kept for analysis after the filtering process. Finally, the remaining vectors from each tracking process are combined to one single file, where they are compared for removing repeated vectors. The combination of these filters neatly aided in obtaining a correct vector map of the flow. These steps assure high confidence and resolution in obtaining the velocity vectors. The average number of instantaneous velocity

vectors within the viewing area of $1cm^2$ is about 1500.

The instantaneous velocity vector fields obtained are then interpolated using the inverse distance algorithm with windows of 20x20 pixels. The final results are instantaneous velocity fields where the vectors are distributed in an ordered grid of 50x50 vectors. To test the influence of the final grid size obtained before the interpolation process, a comparison was performed using the same interpolation technique and different grid sizes. The mean velocity profiles obtained after the interpolation process for grids of 50x50, 75x75 and 100x100 are shown in figure 3. In addition, the streamwise and normal rms velocity components are shown in the figure. It can be observed that there is no significant change in the shape of the velocity profile. The standard deviation of the average velocity obtained using the 75x75 grid with respect to the average velocity obtained using the 100x100 is 0.46 (0.2% difference), while the standard deviation of the average velocity obtained using the 50x50 grid with respect to the average velocity obtained using the 100x100 is 1.13 (0.6% difference).

4. RESULTS AND DISCUSSION

4.1 Statistics

The tests were carried out with a volumetric water flow rates to achieve various Reynolds numbers. The data of the Reynolds number of $Re_H \cong 5128$ based on the half height of the channel, the bulk velocity of 18.3 cm/s, and the viscosity of water will be presented herein.

Figure 4 shows the non-dimensional mean streamwise velocity $U^+ \left(U^+ = \frac{U}{u_\tau} \right)$ profile, versus the non-dimensional y-location, y^+, $\left(y^+ = \frac{y u_\tau}{\nu} \right)$ for single phase flow, and a comparison with data obtained by Warholic[13] in a fully developed channel flow for water at $Re_H = 5100$. The plot is semi-logarithmic and the region near the wall is subdivided between the viscous sublayer which is defined as the region $0< y^+ < 5$. The buffer region is defined by $5< y^+ <30$. This region is the most dynamical region in bounded shear flows. The log region starts at approximately $y^+ = 30$. For $y^+ < 5$ the streamwise non-dimensional velocity agrees with the law of the wall. The solid line passing through the data represents the log law. A good agreement between the theoretical model and the measured data is observed for $y^+ > 30$.

The wall shear stress for single phase was calculated using Eq. (1) and also $\mu \left. \frac{dU}{dy} \right|_{y \approx 0}$ inferred from the measured velocity field using PIV. The derivative was computed with the second order central difference scheme. The wall shear stress values from the two methods are shown in table 1.

It can be observed a reasonable agreement was obtained using the two approaches. The percentage difference between the two methods is about 3.5%. This also gives

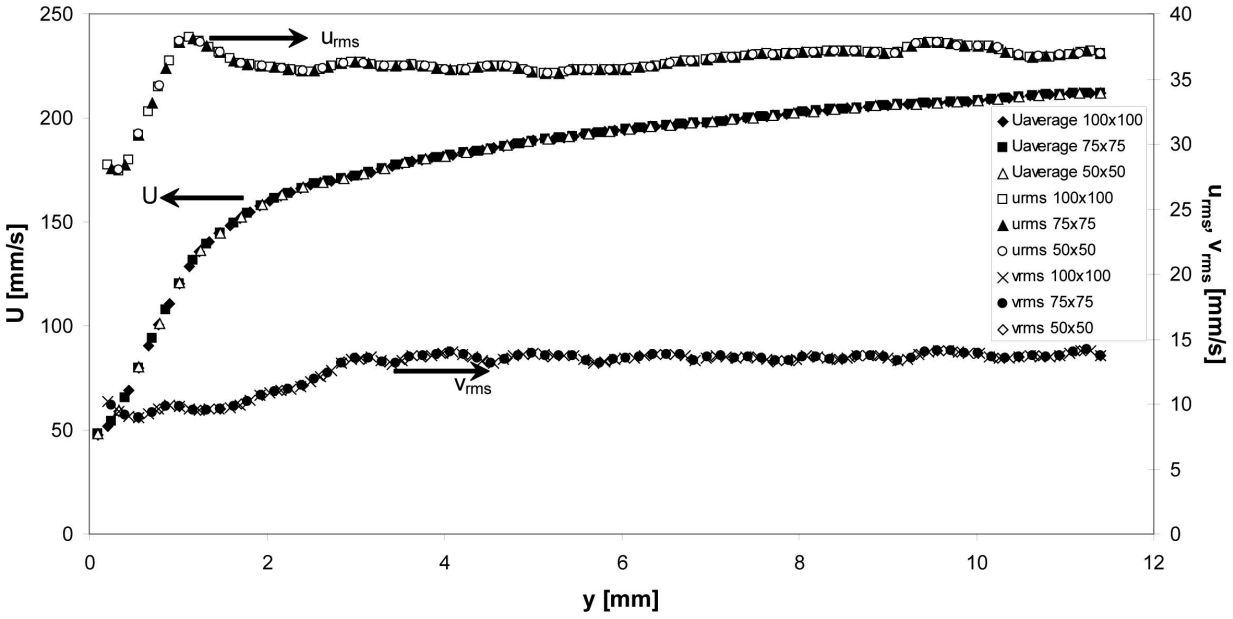

Fig. 3. Single Phase Mean Velocity Profile Obtained Using Three Different Grid Sizes: 50x50, 75x75 and 100x100

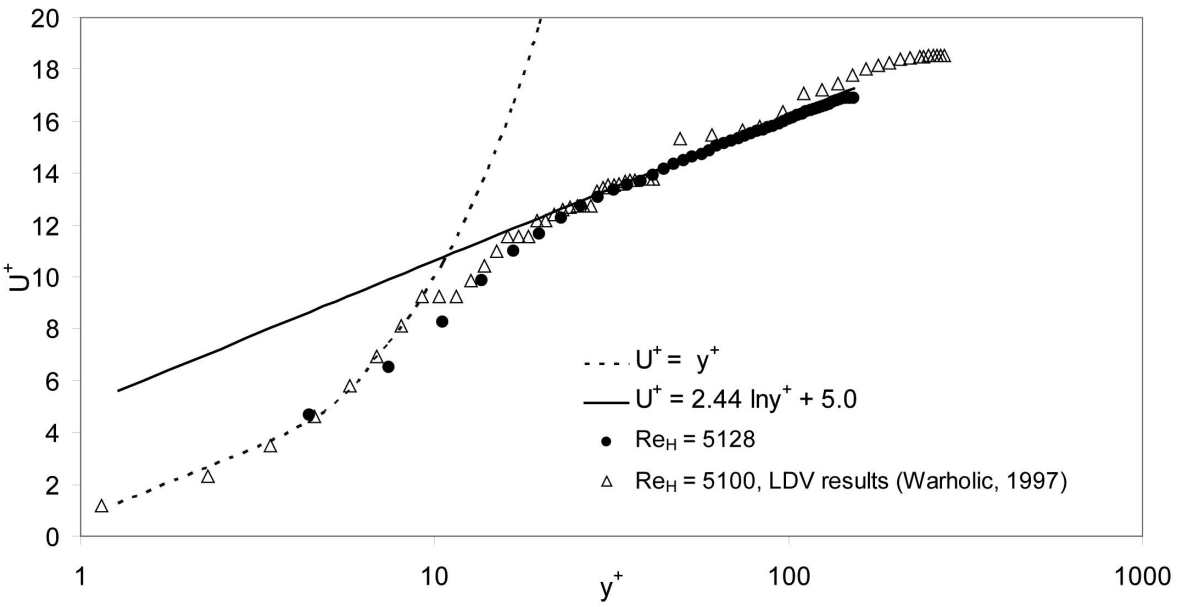

Fig. 4. Non-dimensional Streamwise Velocity, U^+, Versus the Non-dimensional Distance from the Wall, y^+, for Single Phase Flow

Table 1. Comparison of Wall Shear Stress Values for Single Phase

Re_H (Single phase)	τ_w from pressure drop [N/m^2] Eqn. (1)	τ_w from $\mu \left.\frac{dU}{dy}\right\|_{y=0}$ [N/m^2]
5128	0.134	0.139

us confidence in our PIV data. Based on these results, the PIV measurements were used to estimate the shear stress in two-phase flow conditions using the relation $\mu \left.\frac{dU}{dy}\right|_{y\approx 0}$.

The two-phase flow measurements were performed with different void fraction values. The generated bubble size was 30 μm. The void fraction value within the measurement zone was estimated using the following relation:

$$\alpha = \frac{V_g}{V_g + V_l} \tag{2}$$

where V_g , is the volume of the gas bubble in the viewing volume, and V_l is water volume in the viewing volume. It should be indicated that the total value of the void fraction is significantly small that the value given by Equation 2 for local void fraction within the measurement area. The test volume has dimensions of $\Delta x = \Delta y = 11.31$ mm and $\Delta z \cong 1$ mm. The calculated global void fraction was about .001 while the local void fraction can be 5% or less. The drag reduction, DR, is obtained from the following equation $DR = \left[1 - \left(\frac{u_{\tau_{2-phase}}}{u_{\tau_{sin\,gle-phase}}}\right)^2\right]$. The values of the drag reduction with various void fractions for test case of Reynolds number of 5128 are summarized in table 2. The bubble diameter, d, is presented in the wall units; i.e., $d^+ = \frac{du_\tau \rho}{\mu}$ where u_τ is the friction velocity and is given by $u_\tau = \sqrt{\tau_w / \rho}$ where τ_w is the wall shear stress, ρ is the density and μ is the fluid viscosity.

Table 2. Drag Reduction at Various Void Fractions

u_τ [m/s]	0.0108	0.0106	0.0097	0.0091
d^+	0.32	0.31	0.29	0.27
Void fraction (α)	2.4%	3.4%	4.4%	4.9%
Drag Reduction	12%	16%	29.8%	38%

4.2 Fluctuating Velocity Fields

Measurements of the root-mean-square (rms) value (turbulent intensity) for the streamwise velocity fluctuations, in non-dimensional form, u^+_{rms} using the ut, friction velocity are shown in figure 5. Single phase flow case and each of the microbubble two-phase flow cases are normalized by its corresponding friction velocity. It is clear from table 2 that the friction velocity varies with the void fraction values. The friction velocity decreases as the drag reduction increases. The data of Antonia et al. [14] and Warholic [15] for single phase flow measurements are included in figures 5 and 6 for streamwise and normal rms velocity fluctuations, respectively.

The maximum streamwise intensity is located at y^+~13 in the middle of the buffer region, and its value is approximately u_{rms}^+ ~2.55. These values are also in agreement with Fischer et al [16] findings.

A reasonable agreement between the dimensionless rms normal velocity fluctuations and the measurements presented by Antonia was observed. The measurements also agree with Warholic data for $y^+ > 20$. Antonia et al speculated the possibility of the v' measurement contamination from u' within the very close wall region. The resolution is best for $y^+>20$. Jimenez and Pinelli [8] indicated that the region above $y^+=20$ and below $y^+=60$ is important in turbulence autonomous cycle. Fortunately, the measurement in this region has best resolutions. An increase in the magnitude of the non-dimensional rms of streamwise turbulent velocity fluctuations is observed with the drag reduction increase.

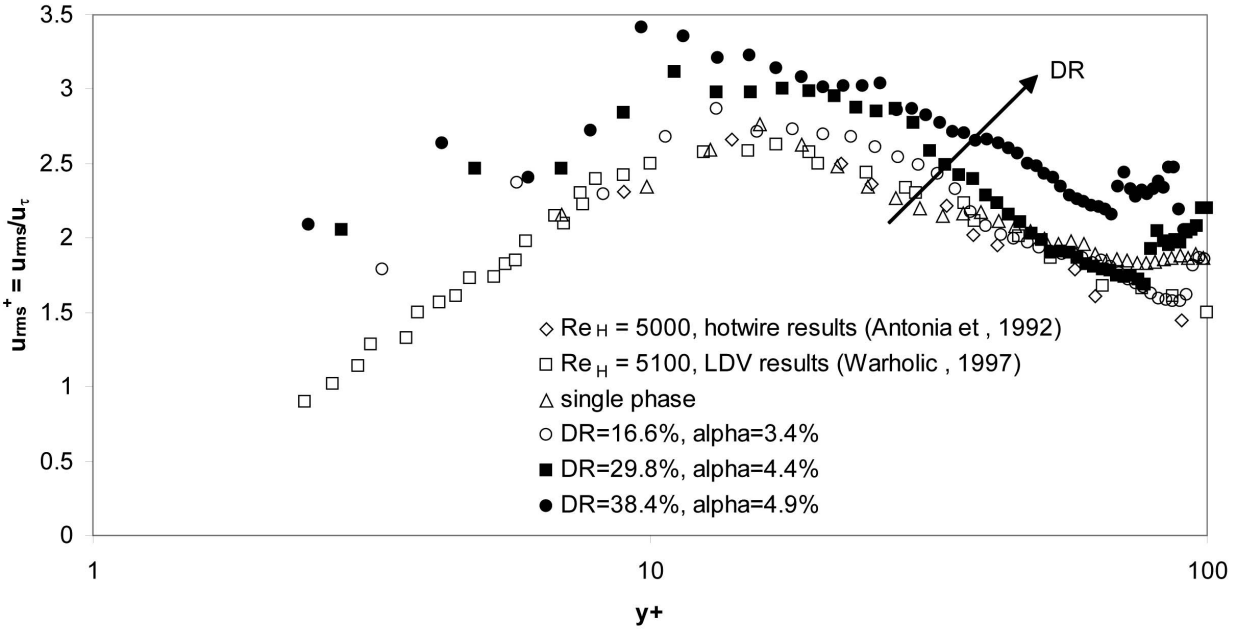

Fig. 5. Non-dimensional Streamwise Turbulent Intensity, Normalized by the Corresponding Friction Velocity

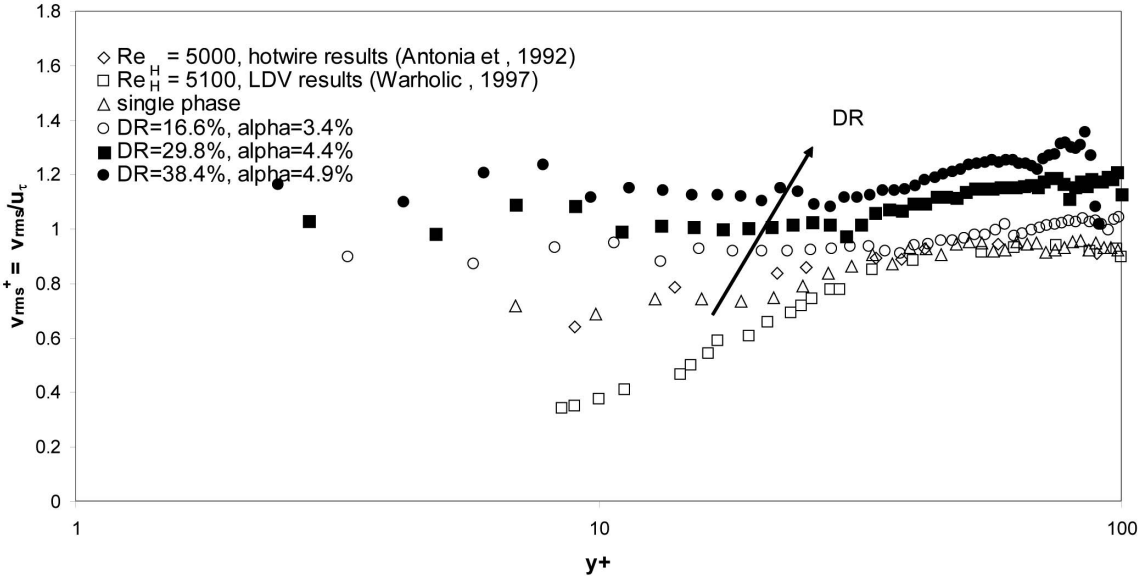

Fig. 6. Non-dimensional Normal Turbulent Intensity Normalized by the Corresponding Friction Velocity

An increase in the magnitude of the non-dimensional normal turbulent intensity is also observed with the increase of the drag reduction (DR). This is elucidated in figure 6. This trend is opposite of the one observed in the results involving drag reduction by polymers injection when the rms normal turbulent velocity fluctuations are normalized with their corresponding friction velocity [17,18,10]. To the knowledge of the authors, this is the first experimental observation of this phenomenon in microbubble drag reduction. It should be noted that the friction velocity is decreasing with the void fraction increase indicating the reduction in the wall shear stress since $u_\tau = \sqrt{\tau_w/\rho}$.

The dimensional rms values of the streamwise and normal velocity fluctuation components are presented in figures 7 and 8, respectively. Single-phase flow and two-phase flow with local void fraction of 4.4% corresponding to drag reduction of about 30% are plotted. The rms velocity fluctuations plots are similar to the previous pesults of reference 19. The presence of polymers produces a decrease in the dimensional rms velocity fluctuations of both streamwise and normal components with the drag reduction (DR) increase. However, it is interesting to note that [15,10] for the same experiment showed an increase in the non-dimensional streamwise intensity, u^+, and a decrease in the non-dimensional normal intensity, v^+, when using the friction velocity u_τ as the non-dimensional parameter.

Similar behavior for the increase in non-dimensional streamwise intensity, u^+, with the increase in the drag reduction is obtained with microbubble drag reduction. However, an increase in the non-dimensional normal intensity is also obtained with the increase of microbubble drag reduction. We found a numerical study of drag reduction with microbubble injection using direct numerical simulation was performed by [9]. They also found out that both rms velocity fluctuations of u and v, normalized by the wall shear velocity increase with the drag reduction for near-wall microbubble injections. This result is presented in figure 7 of their reference. In addition, they indicated that dimensional rms of velocity fluctuation for streamwise component is also reduced near the wall while of those of v is increased near the wall. It is clear that these trends imply that the physical mechanism responsible for the drag reduction via near-wall microbubble injection is different from polymer-induced-drag reduction.

4.3 Reynolds Stresses

Reynolds stresses, for single phase flows, can be obtained from the velocity fields and the values of wall shear stress using the following equation:

$$-\rho\overline{u'v'} = \tau_w\left[1-\frac{y}{H}\right]-\mu\frac{dU}{dy} \qquad (3)$$

where $\mu\frac{dU}{dy}$ is the viscous stress, $-\rho\overline{uv}$ is the Reynolds shear stress, y is the distance from the wall, u' and v' are the fluctuating velocity components of streamwise and normal

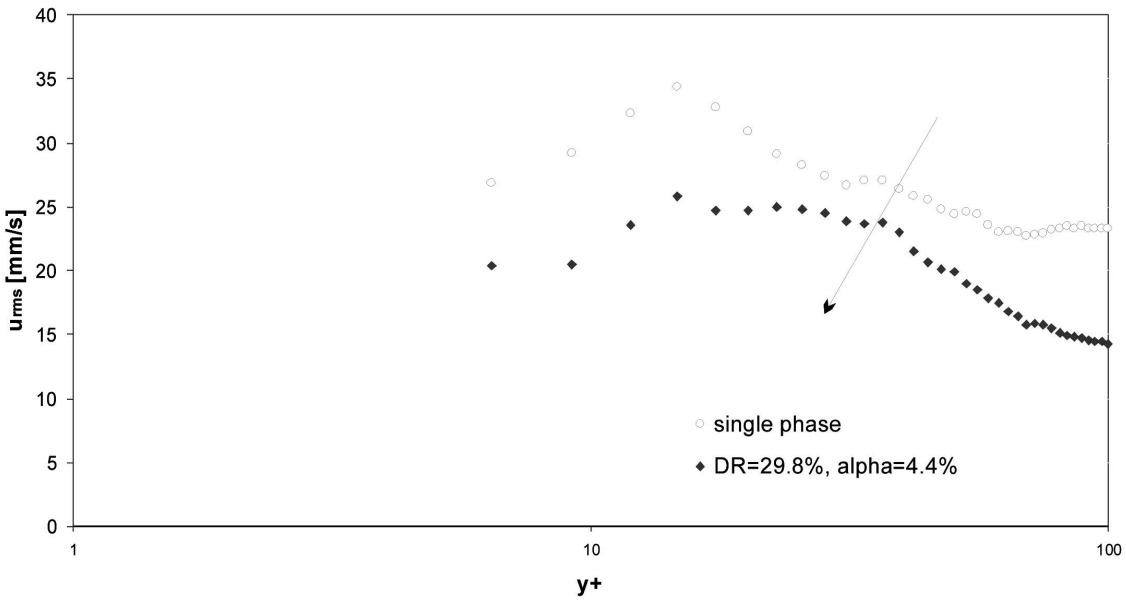

Fig. 7. Dimensional Streamwise Turbulent Intensity

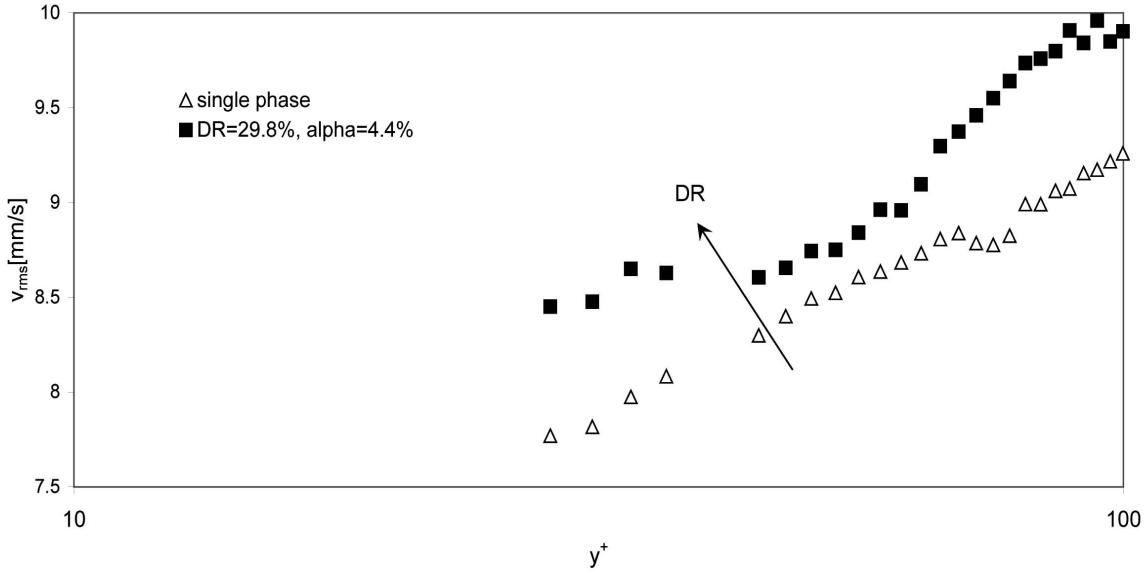

Fig. 8. Dimensional Normal Turbulent Intensity

directions respectively, and U is the average velocity as a function of the distance y. The viscous stress can be obtained from the measured streamwise mean velocity profile. A comparison between Reynolds stresses results directly obtained from PIV measurements and results obtained using eq. (3) is shown in figure 9. The Reynolds shear stress is calculated form PIV using $\overline{u'v'}(x,y) = \frac{1}{N}\sum_{i=1}^{N}\{[u'_i(x,y)][v'_i(x,y)]\}$. A reasonable agreement was observed between the two methods. The standard deviation between of the Reynolds shear stress inferred from PIV velocity data and calculated

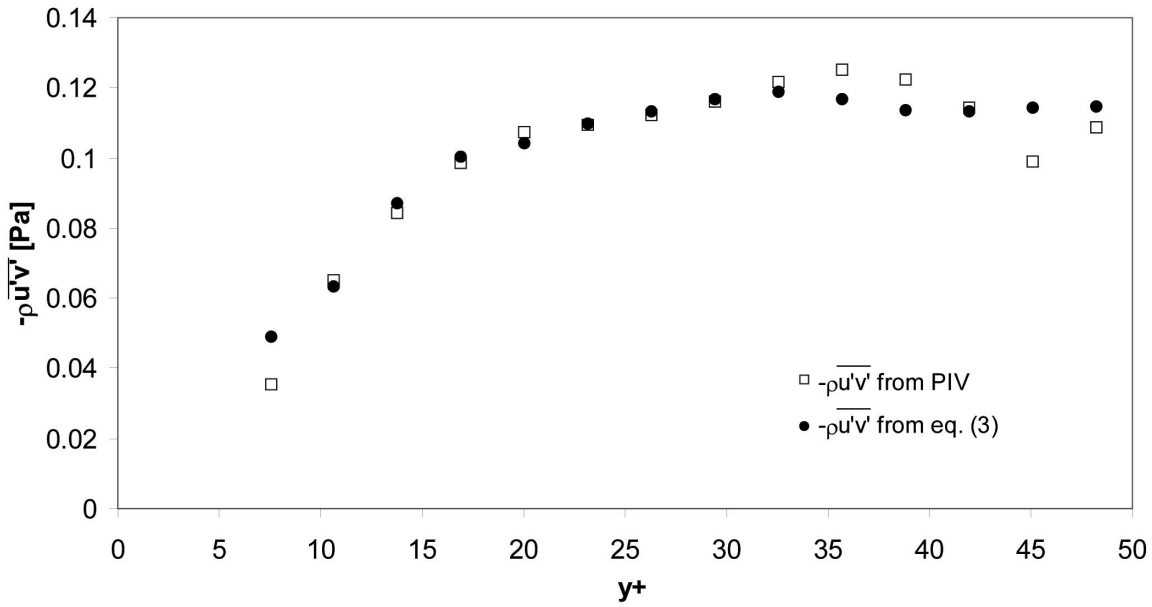

Fig. 9. Comparison Between Values of Reynolds Stresses Obtained by Two Independent Techniques

results using equation (3) is 0.25 and the percentage difference is 6.37%.

Sreenivasan [20] examined measurement of wall-bounded turbulent flow. From a least-square fit of the Reynolds stress peak locations he obtained:

$$y^{+}_{uv,peak} = 2\left(\mathrm{Re}_{\tau}\right)^{0.5} \tag{4}$$

where $y^{+}_{uv,peak}$ is the non-dimensional y-location of the peak Reynolds shear stress and Re_{τ} is the Reynolds number based on the half channel height and the friction velocity ut. The calculated peak location is $y^{+}_{uv,peak} \cong 36$ for $\mathrm{Re}_{\tau} = 325$ which corresponds to the value of $\frac{y}{H} = 0.11$. The location of the maximum value of $-\overline{u'v'}$ from figure 11 is about $\frac{y}{H} \cong 0.11$ for single-phase flow.

Experimental results for Reynolds stresses $-\rho\overline{u'v'}$, obtained from PIV measurements, for various values of local void fractions from 2.4% to 4.9% are shown in figure 10. These results are obtained from the PIV velocity measurements using equation $\overline{u'v'}(x,y) = \frac{1}{N}\sum_{i=1}^{N}\{[u'_i(x,y)][v'_i(x,y)]\}$. The shear stresses are presented as function of, y^{+}, the non-dimensional distance from the wall. A significant decrease in the Reynolds stress with increasing local void fraction is obtained. The presence of the microbubbles within the boundary layer causes a decorrelation between the streamwise, u', and the normal, v', fluctuating velocities. This decorrelation of fluctuating velocities results in a decrease in the Reynolds shear stresses.

Profiles of the Reynolds shear stresses, non-dimensionalized with the square of the corresponding friction velocity for each case are presented in figure 11. It can be observed that despite the normalization, the tendency observed remains the same, as the value of the local void fraction increases, there is a decrease in the Reynolds stresses values.

In order to understand the characteristics of the flows near the wall, the coherent structure within the viewing area could be investigated. The interpretation of vorticity as a tool to get a better understanding of the drag reduction phenomena by microbubble injection is attempted. The concept that the existence of vorticity intensity demonstrates the action of viscous forces on fluid particles; consequently, wall shear stress and vorticity are directly related. When the wall shear stress is high, the vorticity is large. Therefore, a decrease in the wall shear stress is accompanied with a vorticity decrease [21].

4.4 Vorticity Modifications

In this experiment the streamwise (u') and the normal (v') velocity components are measured. Therefore, the spanwise component of the vorticity in the near-wall region was obtained. The z-vorticity component in the near wall region is calculated from:

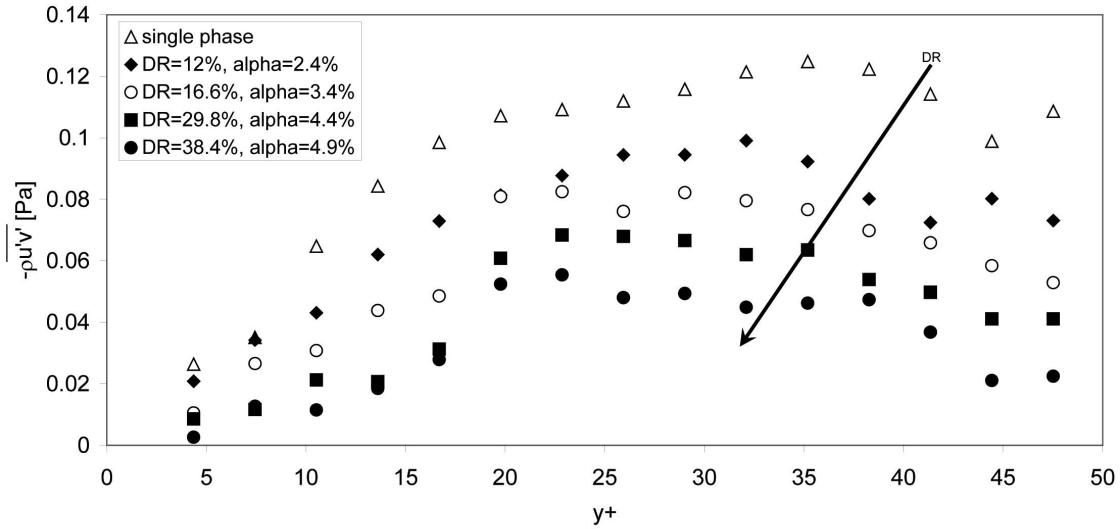

Fig. 10. Reynolds Shear Stress Versus the Normalized Distance from the Wall y^+, for Several Void Fraction Cases

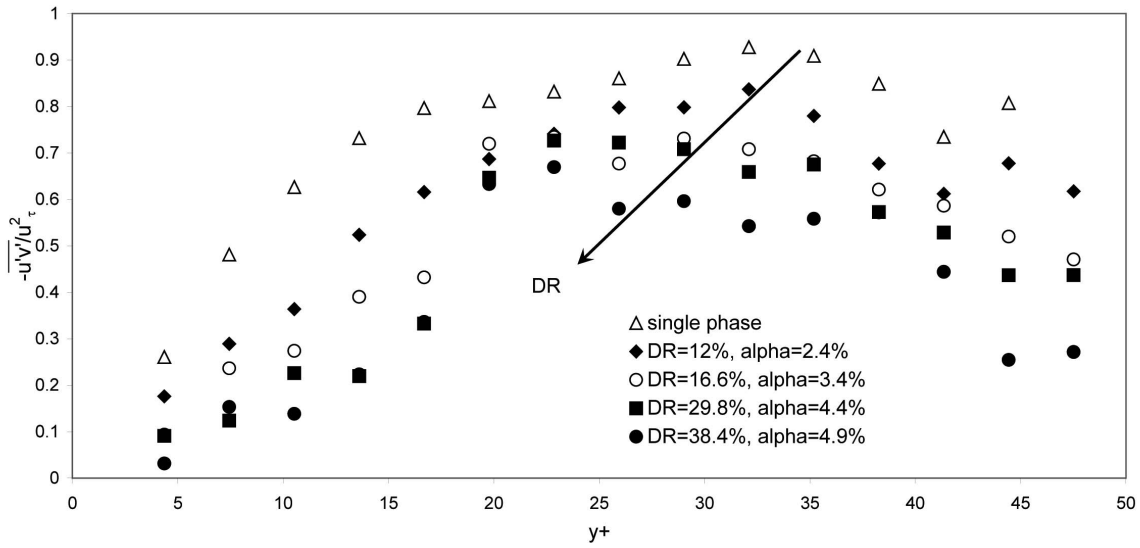

Fig. 11. Non-dimensional Reynolds Shear Stress Versus the Normalized Distance from the Wall y^+, for Several Void Fraction Cases

$$\omega_z = \left(\frac{\partial u'}{\partial y} - \frac{\partial v'}{\partial x} \right) \tag{5}$$

To calculate velocity derivatives, central differences scheme was applied to PIV velocity results. Calculated instantaneous vorticity ω_z from the velocity fields for single-phase flow and two-phase flow with a void fraction of 4.9% are shown in figure 12. It is clear that the vorticity is also affected by the presence of the microbubbles. A significant decrease in the vorticity near the wall is observed with microbubble concentration of 4.9%. The presence of micro-bubbles within the boundary layer produces a decrease in the wall shear stress, and consequently a reduction in the drag. As shown in the Figure (12-a) strong positive and negative vorticities were observed near the wall. Microbubble

injection in the boundary layer suppresses these violent vorticity motion as seen in Fig. 12-b. By examining the other vorticity maps of different void fraction values (2.4%, 3.4%, and 4.4%), not shown here, they also confirm the relationship between the decrease in the vortical structure presence near the wall when microbubbles are present. As void fraction increases, vorticity decreases and this effect is clearly elucidated near the wall. It is also observed that the spanwise component of the vorticity, close to the wall, shows negative values. This region of high vorticity, which is characterized by high dissipation of kinetic energy, is generally surrounded by nearly irrotational fluid with low vorticity. This phenomenon is caused by vortex stretching [22]. Similar behavior has been observed in other studies [23,24].

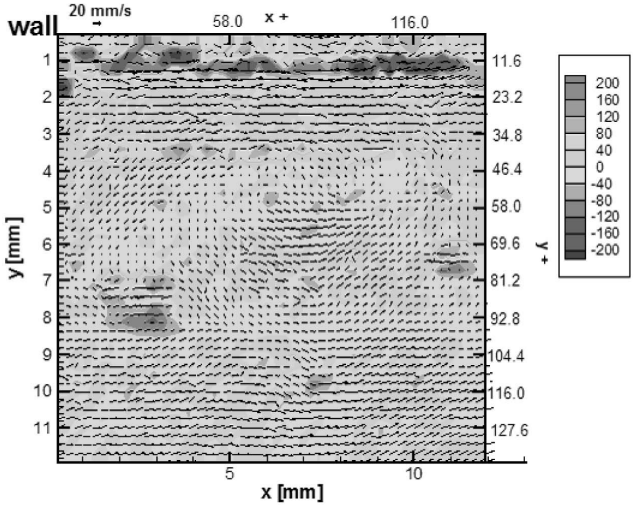

Fig. 12. Z-component of Average Vorticity for a) Single Phase Flow and b) Two Phase Flow α=4.9%, DR=38.4%

4.5 Turbulent Energy

Turbulent energy is generated from the mean flow through an interaction of the turbulent stresses with the mean strain rate. Generally speaking, turbulence production is regarded as a drain of energy from the mean flow to turbulence. The rate of generation of turbulence or turbulence production can be expressed as $\overline{u'_i u'_j} S_{ij}$, where u'_i and u'_j represent fluctuating velocity components and $S_{ij} = \frac{1}{2}\left(\frac{\partial U_i}{\partial x_j} + \frac{\partial U_j}{\partial xi}\right)$ is the mean rate of strain. In this experiment the velocity was measured in the x-y plane. Therefore, the estimation of turbulent energy production for channel flow is obtained from:

$$\text{Turbulent energy production} = -\overline{u'v'}\left(\frac{\partial U}{\partial y}\right) \tag{6}$$

Figure 13 shows the turbulent energy production calculated for single phase flow and microbubble two-phase flows with various local void fraction conditions as a function of the y^+ distance from the wall in the wall units. It is observed that the turbulent energy production decreases as the local void fraction increases. Therefore, as microbubbles are injected into the boundary layer, there is a decrease in the turbulent energy production resulting into a drag reduction. Existence of the microbubbles within the turbulent boundary layer leads to turbulence modulation.

As shown in figure 13 the peak of the turbulence production occurs within the buffer layer. In single phase flow condition, the position for the maximum production rate is comparable to the value of $y^+ \cong 12$, which pointed out for the largest production rate to take place [25].

4.6 Cross Correlation Analysis

Two-point space velocity correlation coefficients for the streamwise and normal components of the fluctuating velocity were carried out due to their usefulness for obtaining direct estimates of the turbulent length scales. The correlation coefficient can be calculated as

$$R_{ij}(\Delta x) = \frac{\overline{u'_i(x)u'_j(x+\Delta x)}}{\sqrt{\overline{u'^2_i}(x)}\sqrt{\overline{u'^2_j}(x+\Delta x)}} \tag{7}$$

The values of the two-point longitudinal correlation coefficients for the streamwise and the normal velocity fluctuations are presented in figures 14-a and 14-b, for single phase and various void fraction conditions at y^+ = 17.4. In addition, figure 15 shows the values of the two-point

transverse correlation coefficients for the streamwise and the normal velocity fluctuations for single phase and various void fraction conditions at $x^+ = 72.4$.

From the figures 14 and 15 it can be observed that for the longitudinal correlation coefficients an increase in the correlation value with the increase of the local void fraction. However, for the transverse velocity correlation coefficients there is a decrease in the correlation magnitude as the local void fraction increases.

The values of the two-point longitudinal correlation coefficients for the streamwise and the normal velocity fluctuations are presented in figures 14-a and 14-b, for single phase and various void fraction conditions at $y^+ = 17.4$. In addition, figure 15 shows the values of the two-point transverse correlation coefficients for the streamwise and the normal velocity fluctuations for single phase and various void fraction conditions at $x^+ = 72.4$.

From the figures 14 and 15 it can be observed that for the longitudinal correlation coefficients an increase in the correlation value with the increase of the local void fraction. However, for the transverse velocity correlation coefficients there is a decrease in the correlation magnitude as the local void fraction increases.

The area under the velocity correlation curve corresponds to the velocity integral length scale. The integral length scale is an average measure of the size of the larger energy

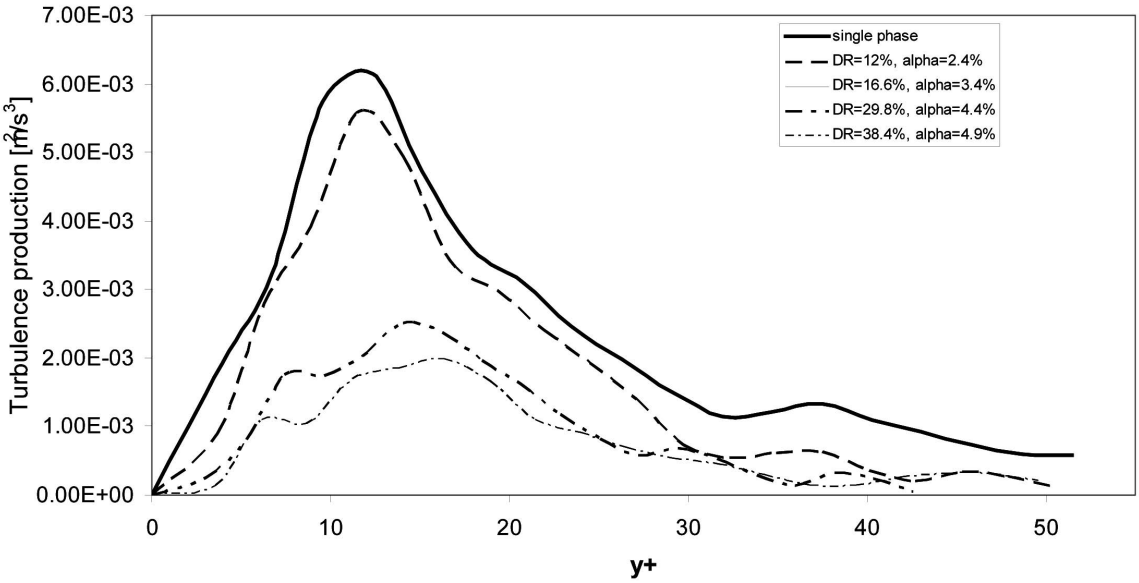

Fig. 13. Turbulent Energy Production for Single Phase Flow and Two Phase Flow with Several Void Fraction Conditions

Table 3. Integral Length Scales for the Longitudinal and Transverse Correlation Coefficients at $y^+ = 17.4$ and $x^+=72.4$

	Longitudinal direction ($y^+ = 17.4$)		Longitudinal direction ($y^+ = 17.4$)	
	L_{uu} [mm]	L_{vv} [mm]	L_{uu} [mm]	L_{vv} [mm]
Single phase	2.05	0.72	1.07	1.36
DR=12.06%, α=2.4%	2.65	0.55	1.53	1.32
DR=16.6%, α=3.4%	2.82	0.44	1.71	1.24
DR=29.8%, α=4.4%	2.88	0.42	2.07	1.22
DR=38.4%, α=4.9%	3.62	0.39	2.26	1.02

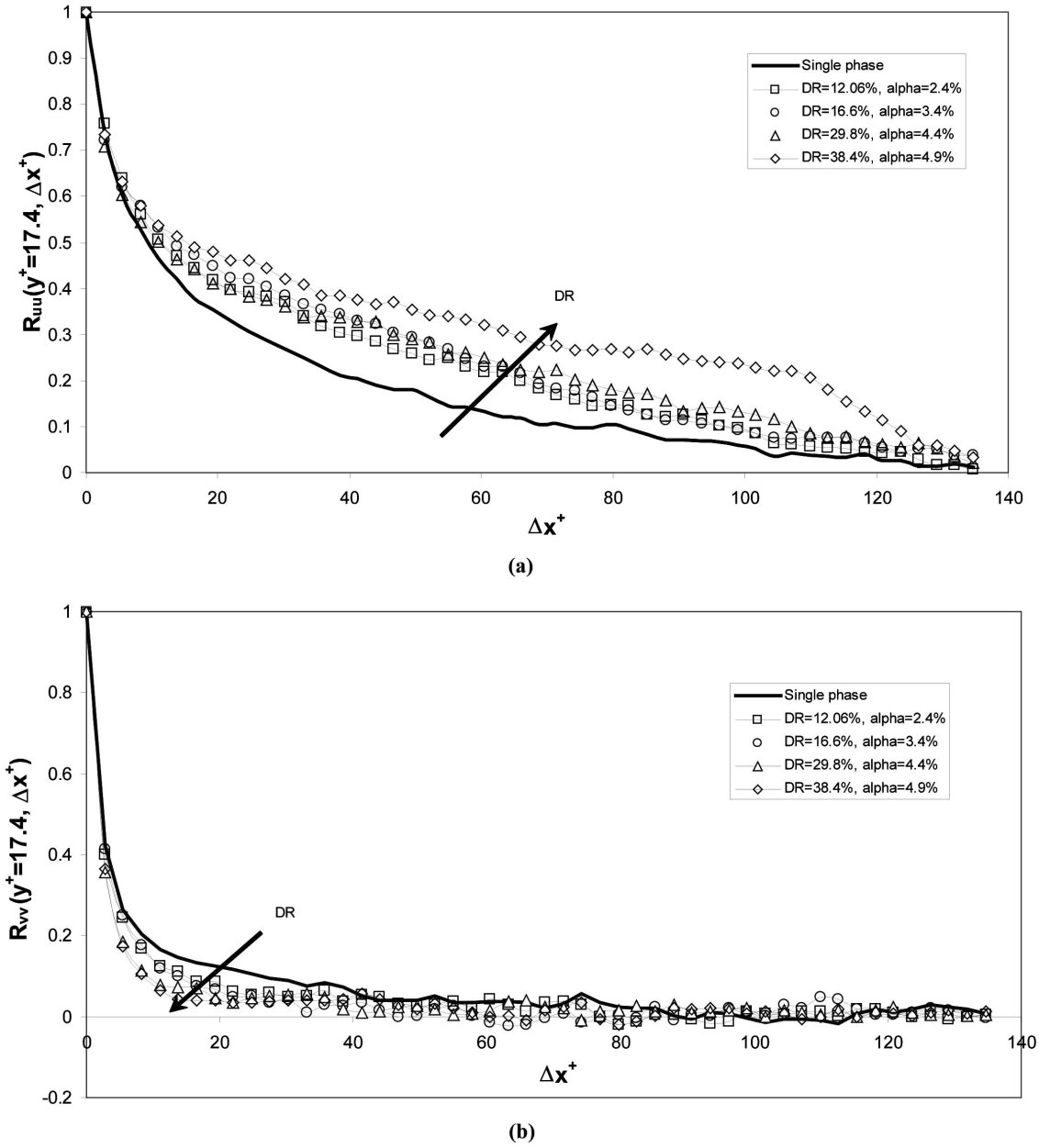

Fig. 14. Correlation Coefficient for a) Streamwise Fluctuating Velocity and b) Normal Fluctuating Velocity at y^+=17.4

containing eddies and it can be calculated from

$$L_i = \int_0^b R_{ij}(\Delta x)dx \qquad (8)$$

where L_i is the integral length scale, R_{ij} is the correlation coefficient function, which depends on the distance Δx, and b is the value of Δx where R_{ij} reaches the first zero value. In these calculations where the correlation coefficient does not reach an absolute zero value, the whole area under the curve is used to calculate the integral length scale. The same formulation is used for the calculation of the integral length scale using the normal fluctuating velocity in both, the longitudinal and the transverse directions. The results of these calculations are shown in table 3.

It can be observed that there is a decorrelation between the streamwise and the normal fluctuating velocity components.

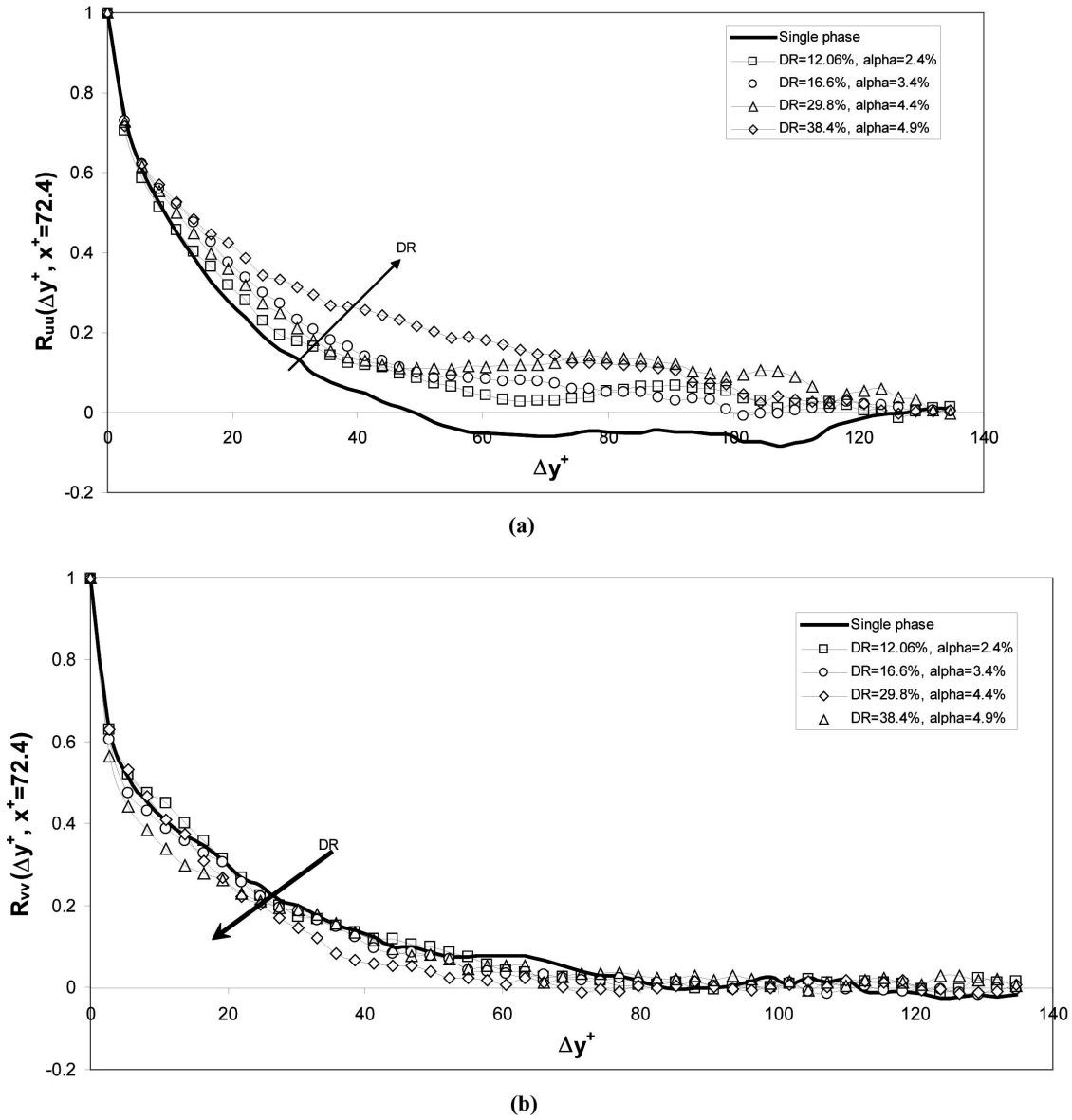

Fig. 15. Correlation Coefficient for a) Streamwise Fluctuating Velocity and b) Normal Fluctuating Velocity at $x^+ = 72.4$

When microbubbles are injected the value of the correlation coefficient decreases drastically compared with single phase flow values. This is particularly true for the buffer layer zone, where the changes in the correlation values are quite significant.

5. CONCLUSIONS

In order to investigate drag reduction caused by microbubbles injection within the boundary layer, in a horizontal channel, the fluctuating velocity components was studied using high resolution PIV technique. An average microbubble diameter of 30 μm was generated via electrolysis. The local void fraction near the upper wall was varied. The presence of the microbubbles within the boundary layer results into a decrease in the Reynolds stress values as the near wall local void fraction is increased. The normalization parameters used to make the rms values of the fluctuating velocities in non-dimensional forms provided different patterns of the velocities profiles. However, these effects are not observed for the normalization of the Reynolds shear stress results. When the rms velocity fluctuations are normalized using

the corresponding friction velocities for each test of the local void fraction cases, an increase in the non-dimensional values of the turbulent intensities as the void fraction increases is observed for both, the streamwise and the normal components. These results contradict the behavior observed in experiments where drag reduction is attained by polymers injection where generally there is a decrease in the magnitude of the turbulent intensities in the normal direction when they are normalized with the corresponding friction velocities. It is clear that there is a decorrelation between the streamwise and normal fluctuating velocity components, which would result into the reduction of drag. This is observed in the uv correlation coefficient results. A reduction of turbulent energy production was also calculated, and with the increase of local void fraction. Degradation in the vorticity layer near the channel wall with the presence of the microbubbles is obtained. The presence of micro-bubbles within the boundary layer seems to act as an agent of vorticity suppression and also causes a modification in the integral length scales.

REFERENCES

[1] McCormick ME; Bhattacharyya R (1973) Drag Reduction of a Submersible Hull by Electrolysis. Naval Engineers Journal 11-16

[2] Madavan NK; Merkle C.L; Deutsch, S (1985) Numerical Investigations into the Mechanisms of Microbubble Drag Reduction. Journal of Fluids Engineering 107: 370-377

[3] Merkle CL; Deutsch S (1989) Microbubble Drag Reduction. Frontiers in Experimental Fluid Mechanics Ced. M. Lecture Notes in Engineering 46: 291-335

[4] Moriguchi Y; Kato H (2002) Influence of microbubble diameter and distribution on fractional resistance reduction. Journal of Marine Science and Technology 7: 79-85

[5] Xu J; Maxey MR; Karniadakis GE (2002) Numerical simulation of turbulent drag reduction using micro-bubbles. Journal of Fluid Mechanics. 468:271-281

[6] Kawamura T; Moriguchi Y; Kato H; Kakugawa A; Kodama Y (2003) Effect of bubble size on the microbubble drag reduction of a turbulent boundary layer, 4th ASME-JSME Joint Fluid Engineering Conference, FEDSM-45645.

[7] Guin MM; Kato H; Yamaguchi H; Maeda M; Miyanaga M (1996) Reduction of Skin Friction by Microbubbles and its Relation with Near-Wall Bubble Concentration in a Channel. Journal of Marine Science and Technology 1: 241-254

[8] Jimenez J; Pinelli A (1999) The Autonomous Cycle of Near-Wall Turbulence. J. Fluid Mech 389: 335-359

[9] Kanai A; Miyata H (2001) Direct numerical simulation of wall turbulent flows with microbubbles. International Journal for Numerical Methods in Fluids 35:593-615

[10] Warholic MD; Heist DK; Katcher M; Hanratty T J (2001) A study with particle-image velocimetry of the influence of drag-reducing polymers on the structure of turbulence. Experiments in fluids. 31: 474-483

[11] Yamamoto Y; Uemura, T; & Kadota, S (2002) Accelerated super-resolution PIV based on successive abandonment method. In Proceedings of 11th International Symposium on Applications of Laser Techniques to Fluid Mechanics.

[12] Hassan Y A; Blanchat T K; Seeley Jr C H (1992) Simultaneous velocity measurements of both components of a two-phase flow using particle image velocimetry. Int J. of Multiphase Flow 18: 371-395

[13] Warholic MD (1997) Modification of turbulent channel flow by passive and additive devices. Ph.D. thesis, University of Illinois.

[14] Antonia, RA; Teitel, M; Kim, J; Browne, LW; (1992) Low-Reynolds-number effects in a fully developed turbulent channel flow. J. Fluid Mech. 236: 579-605.

[15] Warholic, MD; Massah H; Hanratty, TJ (1999) Influence of drag-reducing polmers on turbulence: effects of Reynolds number, concentration and mixing. Experiments in fluids. 27:461-472.

[16] Fischer, M.; Jovanovic', J; Durst, F; (2001). Reynolds number effects in the near-wall region of turbulent channel flows. Physics of Fluids 13: 1775-1767.

[17] Virk PS (1975) Drag reduction fundamentals. AIChE Journal. 21: 625-656

[18] Wei T; Willmarth WW (1992) Modifying turbulent structure with drag-reducing polymer additives in turbulent channel flows. J. Fluid Mech. 245:619-641

[19] Vlachogiannis M; Hanratty TJ (2004) Influence of wavy structured surfaces and large scale polymer structures on drag reduction. Experiments in Fluids. 36: 685-700.

[20] Sreenivasan KR (1988) A unified view of the origin and morphology of the turbulent boundary layer structure in turbulence management and relaminarisation. 37-61. eds Liepmann HW and Narasimha. Springer-Verlag, Berlin.

[21] Panton R L (1996) Incompressible Flow. John Wiley and Sons, Inc.

[22] Lesieur M (1990) Turbulence in Fluids. Kluwer Academic Publishers.

[23] Vukoslavcecic P; Wallas JM; Balint J (1991) The Velocity and Vorticity Fields of a Turbulent Boundary Layer, part 1. Simultaneous Measurements by Hot-Wire Anemometry. Journal of Fluid Mechanics. 228:25-51.

[24] Meng JCS (1998) Wall Layer Microturbulence Phenomenological Model and Semi-Markov Probability Predictive Model for Active Control of Turbulent Boundary Layers. AIAA No. 98-2995.

[25] Bernard PS; Wallace JM; (2002) Turbulent Flow. Analysis Measurement, and Prediction. John Wiley and Sons, Inc.